LA-UR- 00-1028

Title: IMAGING PERFORMANCE STUDIES OF A COMPACT NEAR-INFRARED INTERFEROMETER

Author(s): P. M. McGehee, Gary C. Loos

Submitted to: SPIE Symposium on Astronomical Telescopes and Instrumentation
Munich, Germany
March 27-31, 2000

Los Alamos
NATIONAL LABORATORY

Form 836 (10/96)

DISCLAIMER

DISCLAIMER

Portions of this document may be illegible in electronic image products. Images are produced from the best available original document.

Imaging Performance Studies of a Compact Near-Infrared Interferometer

Peregrine M. McGehee[a] and Gary C. Loos[b]

[a]Los Alamos National Laboratory, Los Alamos, NM, USA
[b]New Mexico Institute of Mining and Technology, Socorro, NM, USA

ABSTRACT

Models of the instrument response and imaging quality are presented for a class of compact near-infrared interferometers. The defining features of this class are 2 to 3 meter diameter telescopes with adaptive optics compensation, 3 to 6 collectors, and relatively short baselines of 50 meters or less. We will also study the effects of having at least one of the collecting apertures moveable along a 100 meter track.

Estimates for the fringe visibilities are derived and the limiting K-band (2.2 micron) magnitudes are computed. Possible science programs are discussed with specific emphasis on the imaging of young stellar object (YSO) accretion disks and optical jets.

Keywords: interferometers, aperture synthesis, YSOs

1. INTRODUCTION

We present design studies of a class of Compact Near-Infrared Interferometers (CNIRI) that bridge the existing sub-r_0 sparse arrays with the 8 to 10 meter based facilities. The defining characteristics of the CNIRIs include the use of moderate apertures with adaptive optics compensation, operations in the near-infrared ($1.0-5.0\mu m$), baselines of order 50 meters, and enhanced filling of the (u,v) plane using the multi-spectral band technique and moveable collectors.

Interferometric arrays are characterized by a set of parameters: N, the number of collecting apertures, D, the diameter of a single aperture, b, the maximum baseline, λ, the wavelength that observations are performed at, and $\Delta\lambda$, the bandwidth centered on λ. The canonical configuration for the CNIRI is presented in the following table.

Table 1. CNIRI configuration.

Parameter	Value
N	3
D	2.5 m
b	50 m
λ	$2.2\mu m$
$\Delta\lambda$ (full)	$0.4\mu m$ (K-band)
$\Delta\lambda$ (narrow)	$0.0125\mu m$

For the CNIRI we will utilize the technique of multi-spectral band observations to enhance the filling of the (u,v) plane given the modest number of baselines. Following Tango and Davis[1] we will use an achromatic geometric phase shifter for modulation of the OPD across the entire set of multi-spectral bands. Each observation will be at a set of spectral bands, defined by a central wavelength λ_k and a width $\Delta\lambda_k$.

Although many details of that the CNIRI design are yet to be completed, we do make a number of assumptions in this analysis. First, that the variation of science object spectral energy distribution (SED) across the K-band

Further author information: (Send correspondence to P.M.M)
Peregrine M. McGehee, MS H820, LANL, Los Alamos, NM 87545. (505) 667-3273 E-mail: peregrine@lanl.gov

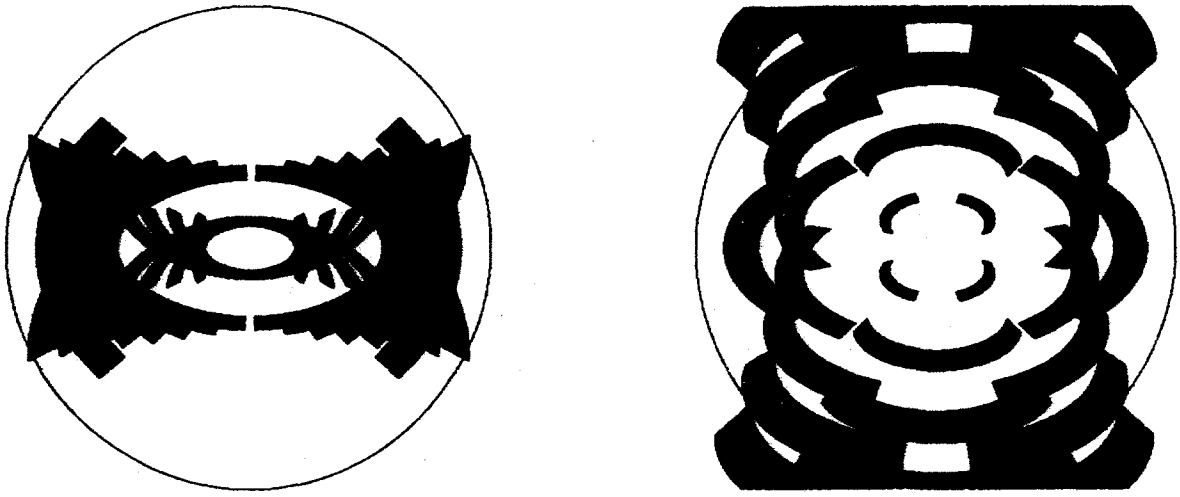

Figure 1. The left-hand figure shows the (u, v) plane coverage for a six hour observation for an object at declination +60 and 32 spectral bands between 2.0 μm and 2.4 μm. The right-hand figure is for a declination of -30 degrees. The observatory latitude is taken as +35 degrees which is typical for the author's location in New Mexico. The circular boundaries indicate the (u, v) limits for a 50 meter projected baseline at $2.2\mu m$.

is taken into account when using multi-spectral band techniques to fill the (u, v) plane. Second, that we are using Michelson beam recombination. Third, that there is no loss in the available photons for fringe detection due to either fringe tracking or Adaptive Optics needs. This implies possible use of a dichoric to separate the light or the use of a reference object (or objects) within the isoplanatic patch.

2. INTERFEROMETRIC IMAGING

We will explore the imaging performance of the CNIRI by examining the resultant (u, v) plane coverage, filling factor, field of view, resolution, map size, and sensitivity. The (u, v) plane coverage and the filling factor describe the completeness of which the source's spatial frequency components are sampled. The range of angular scales covered is set by the field of view, resolution, and image map size. The ultimate limits to faint source detection are defined by the sensitivity to interference fringes.

2.1. (u, v) Plane Coverage

The CNIRI will utilize the techniques of multi-spectral band observations and at least one moveable telescope to mitigate the limitations in (u, v) plane coverage that stem from the use of a small number of collecting apertures. We will primarily deal with partitions of the near-infrared from 2.0 μm to 2.4 μm. The details of these will be dependent on the science goals since it may be advantageous to isolate spectral features such as emission lines.

We will assume the use of only three individual collectors as this is the minimum to acquire closure phase information. One of these will be movable across a N-S track and will have eight equi-spaced stations. Table 2 lists the positions and figure 1 depicts the resultant (u, v) plane coverage.

Table 2. CNIRI station locations.

Station	X (m)	Y (m)
West	-30	0
East	10	0
Mobile	0	$n * (100/7 - 50), n = 0 \ldots 7$

2.2. Filling Factor

We choose to define an operational filling factor q_{obs} that indicates the fractional amount of the (u,v) plane sampled during the course of an observation. This is complementary to the definition given by Roddier and Ridgway[3] which is $q = N(D/b)^2$. In the following analysis we do not include the effect of the large aperture size on the (u,v) plane sampling.

For an observation i of N_{obs} along a single baseline j of N_b and in a spectral band k of N_λ there is a starting point of the (u,v) plane of $\mathbf{u}$ and a movement in the (u,v) plane during the observation of $\Delta\mathbf{u}$. The movement in the (u,v) plane over short time intervals can be approximated by a circular trajectory, thus for an observation time $\tau_{obs,ij}$ and a time of revolution τ_{rev}, the area traversed in the (u,v) plane is

$$A_{ijk} = 2\pi \frac{\tau_{obs,ij}}{\tau_{rev}} \left[\frac{1}{(\lambda_k - \frac{\Delta\lambda_k}{2})^2} - \frac{1}{(\lambda_k + \frac{\Delta\lambda_k}{2})^2} \right] |\mathbf{b}_{ij}|^2. \tag{1}$$

Here $|\mathbf{b}_{ij}|$ is the magnitude of the (u,v) vector for $\lambda = 1$.

The observed coverage of the (u,v) plane over a sequence of observations is then

$$q_{obs} = \frac{2\sum_{i=1}^{N_{obs}} \sum_{j=1}^{N_b} \sum_{k=1}^{N_\lambda} A_{ijk}}{\pi(\frac{b}{\lambda_0})^2} \tag{2}$$

where λ_0 is the reference wavelength for the entire set of observations, defined by

$$\lambda_0 = \frac{\sum_{k=1}^{N_\lambda} \lambda_k}{N_\lambda}. \tag{3}$$

We set all observation times to be the same, hence $\tau_{obs,ij} = \tau_{obs}$ and also specify that the multi-spectral coverage consists of a continguous set of spectral bands bounded entirely by λ_{min} and λ_{max}. Under these conditions, equation (2) becomes

$$q_{obs} = 4\frac{\tau_{obs}}{\tau_{rev}} \left(\frac{\lambda_0}{b}\right)^2 \left[\frac{1}{\lambda_{min}^2} - \frac{1}{\lambda_{max}^2} \right] \sum_{i=1}^{N_{obs}} \sum_{j=1}^{N_b} |\mathbf{b}_{ij}|^2. \tag{4}$$

If we approximate the (u,v) trajectories for a given baseline j as circles about the origin, then $|\mathbf{b}_{ij}| = |\mathbf{b}_j|$ for all observations i and (4) reduces to

$$q_{obs} = 4N_{obs}\frac{\tau_{obs}}{\tau_{rev}} \left(\frac{\lambda_0}{b}\right)^2 \left[\frac{1}{\lambda_{min}^2} - \frac{1}{\lambda_{max}^2} \right] \sum_{j=1}^{N_b} |\mathbf{b}_j|^2. \tag{5}$$

2.3. Field of View

The field of view of an imaging interferometer in Michelson recombination is limited by both the resolution of a single collection aperture ($\theta_D = 1.22\frac{\lambda}{D}$) and the coherence length of light[2] ($\theta_l = (\lambda/b) * (\lambda/\Delta\lambda)$).

For the field of view to be maximal, we design the CNIRI such that $\theta_l > \theta_d$ which sets the field of view as $\theta_{FOV} = \theta_d$. This design criterion places restrictions on the spectral bandwidth $\Delta\lambda$ which must satisfy

$$\Delta\lambda < \lambda\frac{D}{1.22b}. \tag{6}$$

This will impact the use of multi-spectral band filling of the (u,v) plane.

With $D = 2.5m$, $b = 50m$, and $\lambda = 2.2\mu m$, we find that limit to the field of view is 221 mas. The corresponding upper limit of the spectral bandwidth $\Delta\lambda$ is $0.090\mu m$. If the entire 18 percent FWHM K-band is used, then the field of view is limited by the coherence length of light to 50 mas.

2.4. Resolution

The ability of an interferometer to resolve objects is dependent upon the mode of operation. In a model fitting mode we can achieve a much finer resolution at the expense of loss of information about the higher spatial frequency structure of the source.

Interferometric arrays often have their imaging resolution quoted as $1.22\lambda/b$ which is the angular size of an uniform-illuminated disk whose visibility function has it's first zero at a spatial frequency of λ/b. The imaging resolution of the CNIRI in the 50-m configuration is 11.1 mas. This is a first-order approximation since the operational resolution is determined by the effective point spread function (PSF) of the array.

2.4.1. Model fitting

In cases where the source intensity distribution can be expected to conform to a specific model, information can be obtained for objects smaller than the standard imaging resolution parameter. For example, Malbet and Bertout[10] claim detection of an accretion disk when the visibility drops to 0.9. Under their models of Gaussian intensity distribution this corresponds to $0.08 * \lambda/b$ or 15.3 times finer than the resolution stated for imaging.

Therefore the CNIRI can detect Gaussian disks of size 0.73 mas while a baseline of over 700 meters would be required for imaging.

2.4.2. Aperture synthesis

The actual imaging resolution of an interferometer is determined by the effective point spread function (PSF). Unlike filled aperture observations, the PSF is dependent not only on the (u, v) plane coverage but upon the weights assigned to the individual visibility measurements. Thus the imaging performance is not necessarily set at the time of the observations. Under conditions of partially redundant arrays PSF grating rings can conspire to form illusionary sources in the field. For example, the Space Interferometer Mission[2] uses a common spacing of 0.5m which results in a further constraint upon the field of view.

To determine the effective PSF of the synthesized beam we generate the (u, v) plane coverage for a series of observations. We will use the natural weighting procedure where each visibility is given equal weight and the uniform weighting procedure where the weight is the defined as the inverse of the number of observations in a square of side $\Delta u * N_u$. The ensquared energy of the PSF is computed to categorize the extent of the beam halo. Sample PSF and ensquared energy functions are shown in figures 2 and 3 for a 6 hour exposure using natural weighting.

Table 3 lists the 10 percent, 50 percent, and 90 percent ensquared energy box sizes for 6 hour observations at declinations of +60 and -30 in order to study the effects of using natural weighting and uniform weighting with $N_u = 1, 2, 3$. For the CNIRI natural weighting produces the sharpest beam with a 20 mas core and 200 mas halo.

Table 3. Ensquared Energy.

Declination	Weighting	0.10 e.e. (mas)	0.50 e.e. (mas)	0.90 e.e. (mas)
60.0	Natural	14	142	391
60.0	Uniform($N_u = 1$)	42	253	412
60.0	Uniform($N_u = 2$)	97	294	415
60.0	Uniform($N_u = 3$)	76	266	415
-30.0	Natural	21	221	408
-30.0	Uniform($N_u = 1$)	69	291	419
-30.0	Uniform($N_u = 2$)	97	294	415
-30.0	Uniform($N_u = 3$)	80	273	415

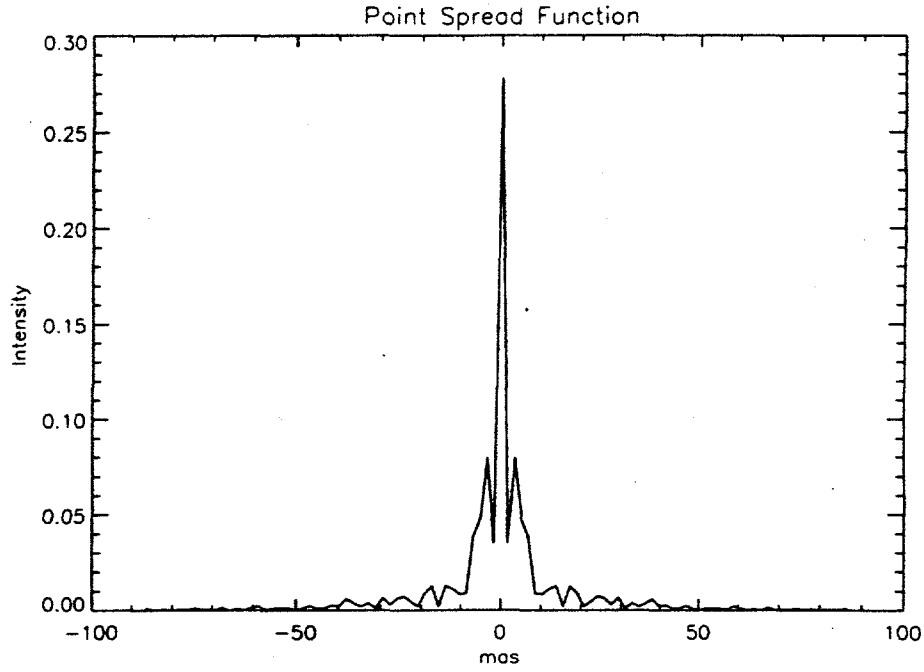

Figure 2. The Point Spread Function for an observation of 6 hours for objects at declination +60 using natural weighting.

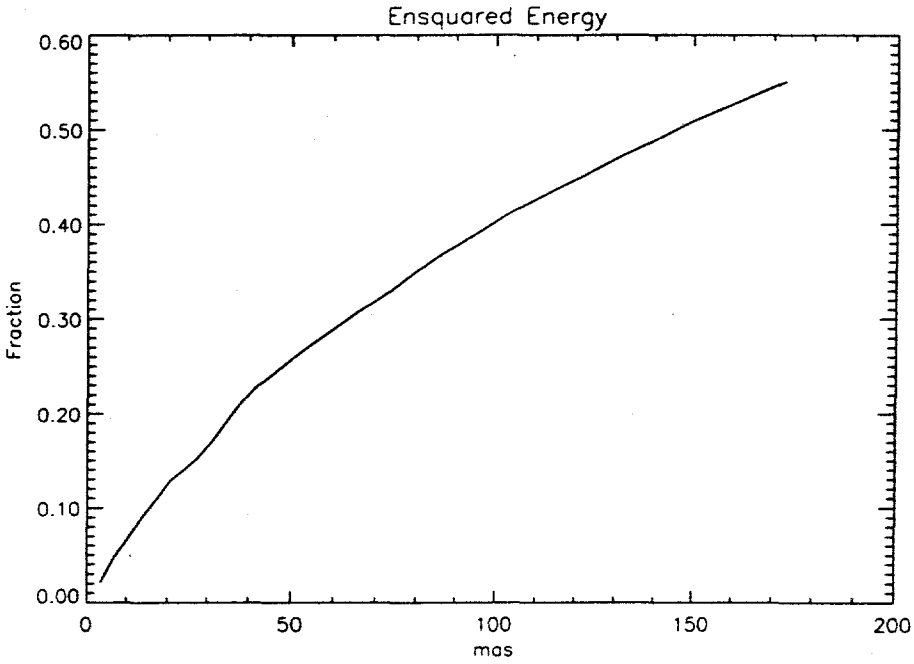

Figure 3. The ensquared energy for an observation of 6 hours for objects at declination +60 using natural weighting.

2.5. Map size

In accordance with standard VLBI techniques[4] we construct the "dirty" map from the interferometric data in the following method. The two independent parameters available for the image synthesis are N_{pix}, the size of the reconstructed image in pixels, and $\Delta\theta$, the image pixel size in radians. We show that these are constrained by oversampling conditions and the field of view.

N_{pix} is size of the reconstructed image. The "dirty" map is written into the central square of length $N_{pix}/2$ to accomodate the requirements of CLEAN. The image pixel size of $\Delta\theta$ results in the (u,v) plane pixel (or bin) size being

$$\Delta u = \frac{1}{N_{pix}\Delta\theta}. \tag{7}$$

Thus the largest baseline (in wavelengths) that can be coped with is

$$u_l = \Delta u \frac{N_{pix}}{2}, \tag{8}$$

where u_l must be greater than the maximum measured baseline (u_{max}).

For CLEAN to properly work and to satisfy the Nyquist condition, we must oversample in the (u,v) plane. The oversampling factor, O, which has the value of 1 at the Nyquist sampling rate, is

$$O = \frac{1}{2u_{max} \times \Delta\theta} \geq O_{min}, \tag{9}$$

where in practice O_{min} should be greater than 2.

We set the extent of the image map to match the field of view, thus

$$N_{pix} = \frac{4\theta_{FOV}}{\Delta\theta} \tag{10}$$

which also sets $\Delta u = 1/(4\theta_{FOV})$. If we insert the maximum value for $\Delta\theta$ derived from the definition of the oversampling factor (9), the constraint on the number of pixels becomes

$$N_{pix} \geq 8u_{max} \times \theta_{FOV} \times O_{min} \tag{11}$$

with the image pixel size determined by (10) as

$$\Delta\theta = \frac{4\theta_{FOV}}{N_{pix}}. \tag{12}$$

If we approximate the (u,v) plane trajectories as circles, then the total integration time per bin in the (u,v) plane is limited by $(24 \times 3600)/(\pi N_{pix})$ seconds.

The minimum number of pixels for the CNIRI in imaging mode as determined by (11) is found to be 390, so rounding up to a power of 2 gives us $N_{pix} = 512$ and $\tau_{pix} = 54$ seconds. The pixel size on the sky is then 1.73 mas which yields 6.4 pixels per imaging resolution element.

2.6. Sensitivity

To determine the sensitivity of the CNIRI, we must determine the standard deviation σ_{V^2} of the squared visibility, or equivalently its signal to noise ratio $SNR_{V^2} = V^2/\sigma_{V^2}$.

We will examine the effect of partial adaptive compensation both with and without the use of single mode optical fibers by extending the treatment by Buscher and Shaklan[5] for SNR_{V^2} with the general approach outlined by Tango and Twiss[6] as well as by Shao[7] for photon noise using Poisson statistics and incorporating a detector and background read-noise term.[12] We also assume the use of the ABCD 4−bin counting technique utilized at PTI and other operational facilities.

2.6.1. Measurement of visibility amplitude

Without the use of single mode optical fibers, the sensitivity is limited by the residual phase variations across the telescope which determine an ensemble average $< V^2 >$ and variance $var(V^2)$ of the squared visibility. We define V_0 as the visibility that would be measured in the absence of atmospheric wavefront aberrations.

$$\sigma^2_{V^2} = \frac{\pi^4}{4MN^4}\left(\frac{V_0^2}{< V^2 >}\right)^2\left[N^2 + \frac{4}{\pi^2}N^3 < V^2 > + \frac{16}{\pi^4}N^4 var(V^2) + 16\sigma^4\right] \tag{13}$$

Here M is the total number of samples in the observation, N is the number of photons per channel per sample, and σ is the RSS of the detector read noise σ_r and the noise due the background blackbody emission σ_b.

When single mode optical fibers are used, the sensitivity is limited by the statistics of the coupling efficiencies into the fibers, given by $< C >$ and $\sigma_C^2 = (< C^2 > - < C >^2)/< C >^2$.

$$\begin{aligned}\sigma^2_{V^2} = \frac{\pi^4}{4MN^4}\left(\frac{1}{< C >^2}\right)\cdot\Bigg[&N^2(1+\frac{\sigma_C^2}{2}) + \frac{4}{\pi^2}N^3V_0^2 < C > (1+\sigma_C)^2 + \\ &\frac{16}{\pi^4}N^4V_0^4 < C >^2(2\sigma_C^2 + \sigma_C^4) + 16\sigma^4\Bigg]\end{aligned} \tag{14}$$

In the zero residual phase variation limit of (13) and in the perfect optical fiber coupling limit of (14) we obtain the performance in the absence of wavefront aberrations.

$$\sigma^2_{V^2} = \frac{\pi^4}{4MN^4}\left[N^2 + \frac{4}{\pi^2}N^3V_0^2 + 16\sigma^4\right] \tag{15}$$

2.6.2. Noise sources

The photon count per channel is derived from the incident spectral flux density F_ν, the width of the channel spectral bandpass $\Delta\lambda$, the system optical efficiency OE, the detector quantum effiency η, the observation time, and the area of the collecting aperture.

$$\begin{aligned}N &= OE \times \frac{\pi D^2}{4} \times \eta\tau_{obs}\int_{band}\frac{F_\nu}{h\nu}d\nu \\ &= K_n \times \eta\tau_{obs}.\end{aligned} \tag{16}$$

To obtain the noise due to the background we integrate the blackbody flux for the ambient temperature over the bandpass. Following Milan-Gabet, et al.,[8] we set the detector acceptance–solid angle product $A\Omega = 4\lambda^2$.

$$\begin{aligned}\sigma_b^2 &= A\Omega \times SE \times \eta\tau_{obs}\int_{band}\left(\frac{1}{h\nu}\right)\frac{2\pi h\nu^3}{c^2}\frac{d\nu}{e^{\frac{h\nu}{kT}}-1} \\ &= K_b \times \eta\tau_{obs}.\end{aligned} \tag{17}$$

where SE is the system emissivity.

The detector read noise σ_r is dependent on the array type, but can be generalized as

$$\sigma_r^2 = K_r \times \tau_{obs}^{n_r} \tag{18}$$

which results in the non-photon noise contribution being $\sigma^2 = K_b \times \eta\tau_{obs} + K_r \times \tau_{obs}^{n_r}$.

As an example, we will compute the sensitivity of the CNIRI with the collecting aperture diameter of 2.5 m and observations in a single narrow-band channel taken as one 32nd of the standard 18 percent FWHM K-band centered at $2.2\mu m$. For imaging we take the oversampling factor $O_{min} = 2$, with a system optical efficiency $OE = 0.1$, and a system emissivity $SE = 1 - OE$. For the detector we choose a NICMOS–3 array with the characteristics of $K_r = 20$, $\eta = 0.6$, and $n_r = 0$.

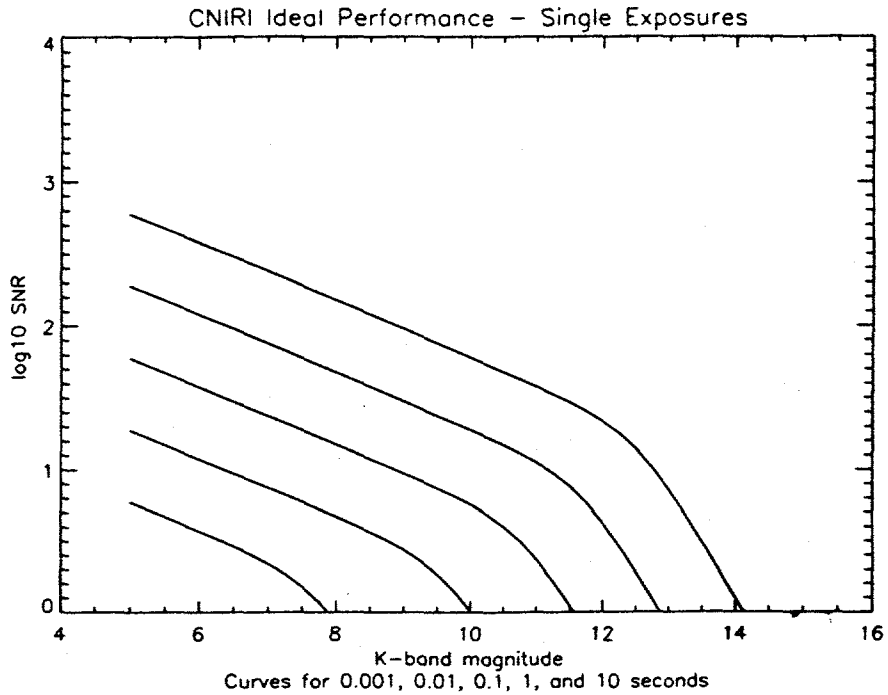

Figure 4. CNIRI SNR_{V^2} performance in the ideal limit for a single narrow-band spectral channel produced by dividing the 18 percent FWHM K-band filter into 32 parts (0.56 percent FWHM).

Under this configuration the photon count and detector+background noise with the background temperature of 293 Kelvin become:

$$N = 3.5 \times 10^7 10^{\frac{-m_k}{2.5}} \tau_{obs} \tag{19}$$

$$\sigma^2 = 3.1 \times 10^3 \tau_{obs} + 20 \tag{20}$$

where m_k is the K−band magnitude of the science object.

Figures 4 and 5 present sample performance data for 0.001, 0.01, 0.1, 1.0, and 10.0 second single exposures under the ideal limit (15). We would enforce a single exposure detection limit at $SNR_{V^2} = 2$.

3. STAR FORMATION STUDIES

We will discuss the ability of the CNIRI to image the accretion disks and the optical jets associated with star formation regions and protostars.

3.1. Accretion Disks

Malbet and Bertout[10] present models of the accretion disks for classical T Tauri stars (CTTS) at 150 pc and for FU Orionis stars at 450 pc. The predicted K-band fluxes are between 1.2 and 16 Jy which map to m_K of 4.0 to 6.8 using the UKIRT photometric system. These can be detected by the CNIRI at a SNR_{V^2} greater than 10^2 even in the narrow-band spectral channel configuration. Although the outer radius of the accretion disks are on the order of 100 AU, the K-band thermal emmission is confined to the central portion of the disk. For CTTS, this is less than 0.1 AU which corresponds to 0.7 mas at a distance of 150 pc. Due to the higher accretion rate, the emission in the FU Orionis disk extends to 0.5 AU which subtends 1.1 mas for a star at 450 pc.

The prospects for imaging and detection of YSO disks are summarized in table 4. It is clear that imaging of accretion disks even for members of the nearby TW Hydrae association[16] will require much longer baselines although the fitting of observed visibilities to models can be accomplished for CTTS systems at distances up to 150 pc.

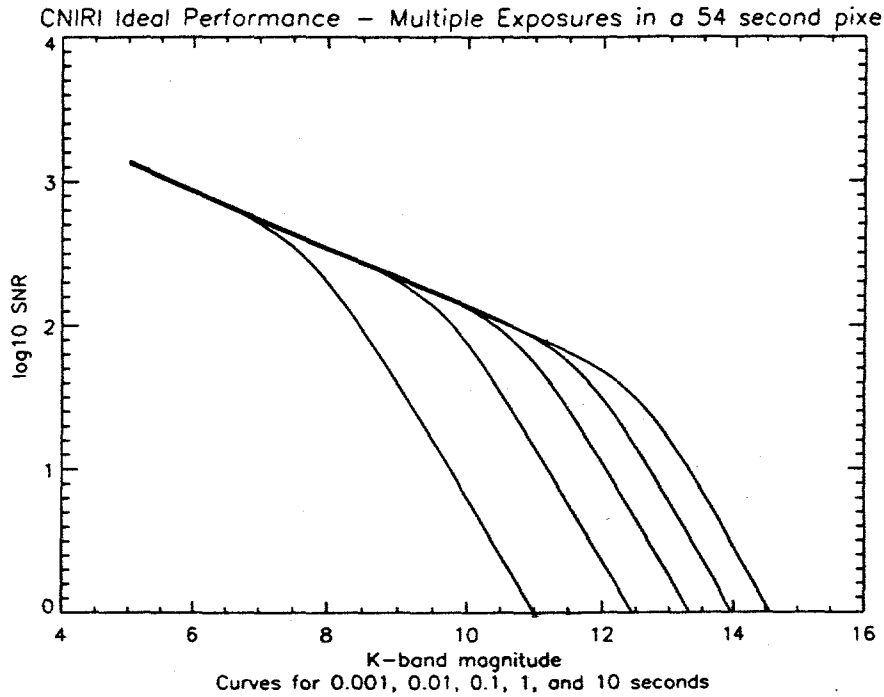

Figure 5. For the same configuration as in figure 4 we show the effect of combining multiple exposures to build one pixel in the (u, v) plane. Note that in this mode extending the integration time of a single exposure helps only in the background limited regime.

Table 4. YSO Accretion Disk Studies

Model	Scale (mas)	Visibility Elements	Imaging Elements
CTTS, 50 pc	2.1	2.9	0.2
CTTS, 150 pc	0.7	0.97	0.07
FU Ori, 450 pc	1.1	1.5	0.10

3.2. Optical Jets

The optical and infrared high-velocity jets from YSOs have characteristic outflow velocities[9] of order 200 km/sec which result in motions of 1.2 AU/day. It is feasible that the CNIRI can be used to advantage in the time-domain by monitoring the changes in jet morphology at the center few AU of the YSO. In the absence of PSF grating ring constraints, the field of view subtends 221 mas which will result in images of the central 33 AU for a YSO at 150 pc.

The baseline results for simulations of the jet formation processes associated with magnetic interaction between the star and the accretion disk performed by Goodson et al.[17] predict jet opening angles of 5 degrees at a distance of 6 AU and 100 degrees at 0.15 AU. The CNIRI will be able to directly image this transition region with a span of 4 to 12 resolution elements for YSOs in the 50 to 150 pc range.

The protostellar jets can be imaged using a single narrow spectral channel centered on the $2.12\mu m$ S(1) v=1-0 line of molecular hydrogen.[9]

4. SUMMARY

The characteristics of a class of near-infrared interferometers have been outlined and possible application to studies of star formation regions has been considered. We anticipate that the combination of adaptive optics and single-mode optical fibers will diminish the residual phase variations across apertures significantly larger than r_0. The gain

in sensitivity from the use of 2.5 m apertures will allow researchers to obtain reasonable signal-to-noise ratios on interference fringe visibilities for sources as faint as $m_K = 14$.

Although the initial baseline of order 50 meters will not permit imaging for objects of angular size less than 11 mas, the successful operation of large phase-stabilized apertures will be a milestone towards deep interferometric imaging at the sub-mas level.

REFERENCES

1. W. J. Tango and J. Davis, "Application of geometric phase techniques to stellar interferometery", *Applied Optics*, **35(4)**, pp. 621-623, 1996
2. T. Boeker and R. J. Allen, "Imaging and nulling with the Space Inteferometer Mission", *astro-ph/9903490*, 1999
3. F. Roddier and S. T. Ridgway, "Filling factor and signal-to-noise ratios in optical interferometric arrays, *University of Hawaii Institute for Astronomy*, **Preprint IfA-99-19**, 1999
4. "CalTech VLBI software documentation - invert", *http://astro.caltech.edu/~tjp/citvlb/vlbhelp/invert.mem*
5. D. F. Buscher and S. B. Shaklan, "Low-order adaptive optics and single-mode fibers in stellar interferometry", **Proc. SPIE Vol. 2201 Adaptive Optics in Astronomy**, p. 980-988, 1994
6. W. J. Tango and R. Q. Twiss, "Michelson Stellar Interferometry, *Progress in Optics, E. Wolf (ed)*, **v17, chap IV**, 1980
7. M. Shao et al., "The Mark III Stellar Interferometer", *Astronomy and Astrophysics*, 1987
8. R. Milan-Gabet, et al, "Signal-to-noise ratio of interference fringe parameters", *IOTA Technical Report*, 1995
9. T. Stanke, M. J. McCaughrean, and H. Zinnecker, "Giant protostellar outflows revealed by infrared imaging", *Astronomy and Astrophysics*, 2000
10. F. Malbet and C. Bertout, "Detecting T Tauri disks with optical long-baseline interferometry", *Astronomy and Astrophysics Supplement Series*, **112**, 369-377, 1995
11. F. Malbet et al., "FU Orionis resolved by infrared long-baseline interferometry at a 2 AU scale", *Astrophysical Journal*, **507**, L149-L152, 1998
12. M. Colavita, "Fringe visibility estimates for the Palomar Testbed Inteferometer", *Proc. Astronomical Society of the Pacific* **111**, 111, 1999
13. C. Haniff and R. Wilson, "Closure-phase imaging with partial adaptive correction". '*Proc. Astronomical Society of the Pacific*, **1006**, 1003-1014, 1994
14. L. Hartmann, "Accretion Processes in Star Formation", *Cambridge: Cambridge University Press*, 1998
15. F. Roddier, "Adaptive Optics in Astronomy", *Cambridge: Cambridge University Press*, 1999
16. D. A. Weintraub et al., "NICMOS narrow-band infrared photometry of TW Hya association stars", *astro-ph/0002078*, 2 Feb 2000
17. A. P. Goodson, K.-H. Bohm, and R. M. Winglee, "Jets from accreting magnetic young stellar objects: I. Comparison of observations and high-resolution simulation results", *Astrophysical Journal*, **154**,142-158, 1999 October 10